THE EUROPEAN
PHYSICAL JOURNAL
SPECIAL TOPICS

Review

Mn *K* edge resonant X-ray scattering of half-doped manganites

J. Herrero-Martín[1,a], J. García[2,a], J. Blasco[2], and G. Subías[2]

[1] Institut de Ciència de Materials de Barcelona-CSIC, Campus Universitari de Bellaterra, 08193 Bellaterra, Spain
[2] Instituto de Ciencia de Materiales de Aragón, Departamento de Física de la Materia Condensada, CSIC-Universidad de Zaragoza, 50009 Zaragoza, Spain

Abstract. We here revisit the concepts of the so-called charge and orbital order in half-doped manganites through the analysis of recent resonant X-ray scattering experiments at the Mn K edge on three different systems: $Nd_{0.5}Sr_{0.5}MnO_3$, $Bi_{0.5}Sr_{0.5}MnO_3$ and $La_{0.5}Sr_{1.5}MnO_4$. By means of a semiempirical method and *ab initio* multiple scattering calculations we conclude that the description of the charge-localized phases is consistent with a model where two Mn atoms are occupying different crystallographic sites (Mn1, Mn2) displaying an electronic occupation that is mainly determined by the structural distortions. Regarding the local structure of these Mn sites, these distortions produce little variations on the charge density associated to the different crystallographic sites. Accordingly, the resulting bimodal distribution of charges is in all cases far from the theoretical arrangement of integer valence states.

1 Introduction

The tuning of synchrotron radiation has allowed developing new X-ray diffraction techniques such as resonant X-ray scattering (RXS). RXS consists on recording the intensity of a Bragg reflection as a function of the energy of the scattered photons by crossing an atomic absorption edge [1] . Due to the fact that absorption edge energies (E_{res}) are specific to a particular atom and to a particular electronic level [2], RXS has atomic and spatial selectivity. This technique combines absorption and diffraction as the X-ray atomic *anomalous* scattering factor is intimately related to the X-ray absorption coefficient. Therefore, it provides local information on the set of long range ordered atoms selected by the diffraction condition and it is chemical, valence and site specific. This technique can be applied to study any Bragg reflection. When the reflection is intense (i.e. the Thomson scattering is important), the anomalous term induces small modulations of the scattered intensity as a function of the photon energy. This is addressed by DANES (diffraction anomalous near edge

---

[a] e-mail: `jherrero@icmab.es; jgr@unizar.es`

structure) and DAFS (diffraction anomalous fine structure) techniques [3,4], in analogy to well known XANES (X-ray absorption near edge structure) and EXAFS (extended X-ray absorption fine structure) techniques. The term RXS is generally used for the study of superlattice reflections, both weak permitted (i.e. with a low Thomson scattering intensity) or *forbidden* by the cell symmetry. In this case the dependence of the reflected intensity on the photon energy mainly reflects variations in the atomic anomalous scattering factor presented by a specific atom (selected by the photon energy of its absorption edge). Since the structure factor of forbidden (or nearly forbidden) reflections is basically given by the difference of the atomic scattering factor (ASF) of a single atomic species in the lattice, these reflections only appear (or their intensities are dramatically enhanced/reduced) in a very narrow region of photon energies (several eV). By the resonance term we mean the RXS spectral features that may appear at the absorption edge where the contrast in the anomalous part of the scattering factors is maximum. The atomic anomalous scattering factor depends on the local geometric structure and the chemical state of the selected atom. Therefore, RXS informs us on the spatial arrangement of charges and the anisotropy of selected atoms, generically referred to as charge order (CO) and orbital order (OO), respectively. Thus, RXS has been employed for the study of the CO and OO phenomena in transition metal oxides either in the hard X-ray [5–9] or the soft X-ray regime [10–13]. Pioneering RXS experiments on manganites were performed by Murakami et al. in $La_{1.5}Sr_{0.5}MnO_4$ and $LaMnO_3$ [6,7], which were considered as a proof of ionic order Mn^{3+}-Mn^{4+} and Mn^{3+} $3d$-orbital order. This interpretation was later criticized by a more detailed quantitative data analysis, showing that the CO cannot be ionic and the OO is originated in the anisotropy induced by the local structure [14–20]. Here, we revise our RXS [14–18] results on the so-called CO phase in half-doped manganites and present a common description for the RXS data. We will show that the observed phenomenology is well explained on the basis of changes in the local structure around the Mn atom, originated in the softening of some phonon modes.

In this contribution, i) we recall the theoretical basis of the resonant X-ray scattering amplitude; ii) we then restrict to the Mn K edge and to the dipole-dipole channel which accounts for most of the phenomenology; iii) we discuss the energy, polarization and azimuth dependence; iv) we classify the reflections responsible for the appearance of RXS spectra of doped manganites as CO and ATS (anisotropy of the tensor of susceptibility) [21]; v) we present a semiempirical approach and *ab initio* multiple scattering calculations by the FDMNES code [22]. Finally, we devote the conclusions section to discuss the different approaches performed and to describe the low temperature structure.

2 Theory of resonant X-ray scattering [23, 24]

The coherent elastic X-ray diffraction on a single crystal is given by the interference of the individual atomic scattering amplitudes at different lattice sites. The measured intensity is given by the square of the structure factor which is given by:

$$F = \sum_j e^{i\vec{Q}\cdot\vec{R}_j}(f_{0j} + f'_j + if''_j) \tag{1}$$

where $\vec{R}_j$ is the position of the j-scattering atom in the unit cell, $\vec{Q} = \vec{k}^f - \vec{k}^i$ is the scattering vector ($\vec{k}^i$ and $\vec{k}^f$ are the wave vectors of the incident and scattered beams) and f_{0j} is the Thomson scattering part of the scattering factor of the j-atom.

The resonant (or anomalous) part, $f' + if''$, is given by the expression [23]:

$$f' + if'' = \frac{m_e}{\hbar^2} \frac{1}{\hbar\omega} \sum_n \frac{(E_n - E_g)^3 \langle \psi_g | \hat{O}^{f*} | \psi_n \rangle \langle \psi_n | \hat{O}^i | \psi_g \rangle}{\hbar\omega - (E_n - E_g) - i\frac{\Gamma_n}{2}}. \tag{2}$$

Here, $\hbar\omega$ is the photon energy, m_e is the electron mass, ψ_g describes the initial and final electronic states with energy E_g, and E_n and Γ_n are the energy and inverse lifetime of the intermediate excited states ψ_n. The interaction of the electromagnetic radiation with matter is expressed by the operators $\hat{O}^i$ and $\hat{O}^{f*}$. By multipole expansion of these operators up to the electric quadrupole term (we can neglect higher order multipoles in most of the cases), we obtain [20]:

$$\hat{O}^{i(f)} = \vec{\varepsilon}^{i(f)} \cdot \vec{r} \left(1 - \frac{1}{2} i \vec{k}^{i(f)} \cdot \vec{r} \right) \tag{3}$$

with $\vec{r}$ the electron position measured from the absorbing atom and $\vec{\varepsilon}^{i(f)}$ being the polarization of the incident (scattered) beam. This permits to separate the resonant part of the ASF into three contributions: dipole-dipole (dd), dipole-quadrupole (dq) and quadrupole-quadrupole (qq).

Thus, Eq. (2) can be written in a Cartesian coordinate frame in the form:

$$f' + if'' = \frac{m_e}{\hbar^2} \frac{1}{\hbar\omega} \sum_n \frac{(E_n - E_g)^3}{\hbar\omega - (E_n - E_g) - i\frac{\Gamma_n}{2}}$$
$$\left[\sum_{\alpha,\beta} \varepsilon_\alpha^{f*} \varepsilon_\beta^i D_{\alpha\beta} - \frac{i}{2} \sum_{\alpha\beta\gamma} \varepsilon_\alpha^{f*} \varepsilon_\beta^i (k_\gamma^i I_{\alpha\beta\gamma} - k_\gamma^f I_{\beta\alpha\gamma}^*) + \frac{1}{4} \sum_{\alpha\beta\gamma\delta} \varepsilon_\alpha^{f*} \varepsilon_\beta^i k_\gamma^f k_\delta^i Q_{\alpha\beta\gamma\delta} \right] \tag{4}$$

where $\alpha, \beta, \gamma, \delta$ are indices that vary independently over the three Cartesian directions x, y, z, and the transition matrix elements $D_{\alpha\beta}$, $I_{\alpha\beta\gamma}$ and $Q_{\alpha\beta\gamma\delta}$ associated to dd, dq and qq contributions are characterized by the following Cartesian tensors of second, third and fourth rank, respectively:

$$D_{\alpha\beta} = \sum_n \langle \psi_g | r_\alpha | \psi_n \rangle \langle \psi_n | r_\beta | \psi_g \rangle$$

$$I_{\alpha\beta\gamma} = \sum_n \langle \psi_g | r_\alpha | \psi_n \rangle \langle \psi_n | r_\beta r_\gamma | \psi_g \rangle$$

$$Q_{\alpha\beta\gamma\delta} = \sum_n \langle \psi_g | r_\alpha r_\beta | \psi_n \rangle \langle \psi_n | r_\gamma r_\delta | \psi_g \rangle.$$

If we restrict to the dipole-dipole main contribution, the atomic anomalous scattering factor is a two-range tensor. In this case and in contrast with Thomson scattering (which is a scalar term) the structure factor becomes:

$$F = \boldsymbol{\varepsilon} F_{\alpha,\beta} \cdot \boldsymbol{\varepsilon}', \text{ where } F_{\alpha,\beta} = \sum_i f_{\alpha,\beta}^i \cdot e^{-2\pi i (Q \cdot r_i)}$$

where $F_{\alpha,\beta}$ and $f_{\alpha,\beta}^\iota$ are symmetric tensors in the absence of magnetic scattering. Consequently the measured intensity of reflections depends on the polarization of the incident and the scattered beam (σ indicates that $\boldsymbol{\varepsilon}$ is perpendicular to the scattering plane and π corresponds to ε contained in it), on the azimuthal angle (referring to a rotation around the $\boldsymbol{Q}$ vector) and on the energy of incoming photons. Therefore, the RXS scattering of a particular reflection contains richer information than the Thomson (i.e. at $E \neq E_{\text{res}}$) scattering.

As we commented before, RXS is mainly useful to study either low intensity or forbidden (by the crystal cell symmetry) reflections. In both cases the structure factor contains the differences between the ASF of the same atomic species localized in different crystallographic sites.

In the first case, the crystallographic sites of the involved atoms are non-equivalent and consequently, the atomic anomalous scattering tensors are different. The main differences come from valence dissimilarities and they are interpreted as due to a charge disproportion. The valence is highly correlated with the metal-ligand bond lengths. These reflections have been extensively analyzed by approaching the atomic scattering tensor to a scalar, but sometimes this approximation is inappropriate [15]. We note that a scalar description implies the absence of azimuthal and polarization dependences. In order of this approach to be valid, no azimuthal dependence should be observed.

In the second case, the lattice sites occupied by the involved atoms are crystallography equivalent but they are related by symmetry operations including a translation (screw axis and/or glide plane). If the tensor scattering is anisotropic these symmetry operations change the sign of some of the out-of-diagonal terms of the scattering tensor producing that the resulting ASF tensor counts on some non-zero out-of-diagonal terms. These are ATS (anisotropy of the tensor susceptibility) reflections and they show marked azimuthal and polarization dependences. Many works describe these reflections as OO reflections, suggesting that they are due to the local anisotropy induced by an ordering of electronic orbitals [6–8,10,11,13].

3 Half-doped manganites

Mixed valence manganese oxides with perovskite structure have been a matter of intense research because of their singular properties [25,26]. Particular attention has been paid to the so-called half doped manganites. In this case, by simple inspection of the integral valence of the constituents, the formal valence of the manganese atoms is 3.5. These compounds include "tridimensional" (3D) pseudocubic manganites as $La_{0.5}Ca_{0.5}MnO_3$, $Nd_{0.5}Sr_{0.5}MnO_3$ and $Bi_{0.5}Sr_{0.5}MnO_3$ or "bidimensional" (pseudo-2D) layered ones as $La_{0.5}Sr_{1.5}MnO_4$. On lowering temperature, all these compounds undergo a semiconductor-insulator transition at a temperature T_{SI} that was described as a CO transition. It has been argued that above T_{SI}, the lattice sites are dynamically occupied by Mn^{3+} and Mn^{4+} ions whereas below this temperature the ions order in a periodic arrangement [27]. Figure 1 shows the *checkerboard* order proposed for these compounds, which allows the orbital ordering of Mn^{3+} $3d$ e_g electrons to rise in addition to the ionic ordering.

In the case of 3D perovskites (orthorhombic *Pbnm*) [28] $(h,0,0)$ and $(0,k,0)$ periodicities with h, k odd, appear because of the supposed ionic periodicity (CO) and $(0,k/2,0)$ of the argued orbital ordering (OO) periodicity with $k/2$. For the pseudo-2D $La_{0.5}Sr_{1.5}MnO_4$ perovskite the new periodicities will have $(h/2,h/2,0)$ and $(h/4,h/4,0)$ indices relative to the tetragonal symmetry $I4/mmm$ [18,29,30]. The structure factor of these modulations contains, for CO reflections, the differences between the atomic scattering tensors of formal Mn^{3+} and Mn^{4+} ions, whereas OO modulations show differences between the same type of atoms (Mn^{3+}) in consecutive cells.

In the following, we focus on some representative compounds: $Nd_{0.5}Sr_{0.5}MnO_3$ (NSMO), $Bi_{0.5}Sr_{0.5}MnO_3$ (BSMO), and $La_{0.5}Sr_{1.5}MnO_4$ (LSMO). Within the Ruddlesden-Popper nomenclature for layered perovskites with general formula $AO(ABO_3)_n$, the first two 3D-manganites correspond to $n \to \infty$ and the latter pseudo-2D to n = 1. The RXS spectra we present in the following were all recorded
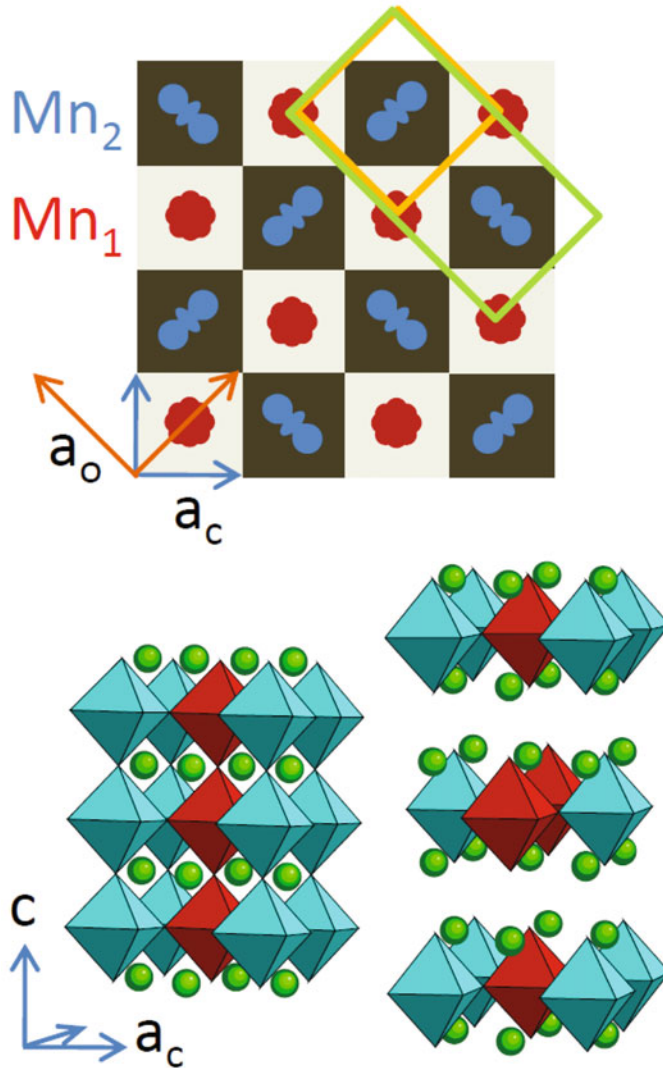
Fig. 1. Schematic view of the crystal structure of CO manganites. In the top, the checkerboard array of Jahn-Teller distorted Mn^{3+} and nearly isotropic Mn^{4+} ions within the ab plane of the perovskite. The orange and green lines denote the unit cell by considering CO and both CO-OO order, respectively. In the bottom we show the distribution of Mn atoms in the cell for a cubic (left) and a single-layered (right) perovskite, corresponding to n $\rightarrow \infty$ and n = 1 in the Ruddlesden-Popper series, respectively.

on single crystals at the ID20 beamline of the ESRF, in Grenoble, France. In Fig. 2 we depict the basic elements characterizing the experimental configuration used. More details can be found elsewhere [15, 16, 18].

The energy dependence of the measured intensity of $\boldsymbol{Q} = (0, k, 0)$ (k odd) reflections at the Mn K edge in pseudo-cubic perovskites and the equivalent $(h/2, h/2, 0)$ (h odd) reflections in $La_{0.5}Sr_{1.5}MnO_4$ are shown in Fig. 3. Non-resonant intensity is found far from the Mn K edge region while at the absorption edge a broad resonance arises in $(0,k,0)$ reflections in the non-rotated $(\sigma - \sigma')$ channel. Also, as the inset in Fig. 3(b) shows, the intensity variation with the azimuth (at the resonance) follows a
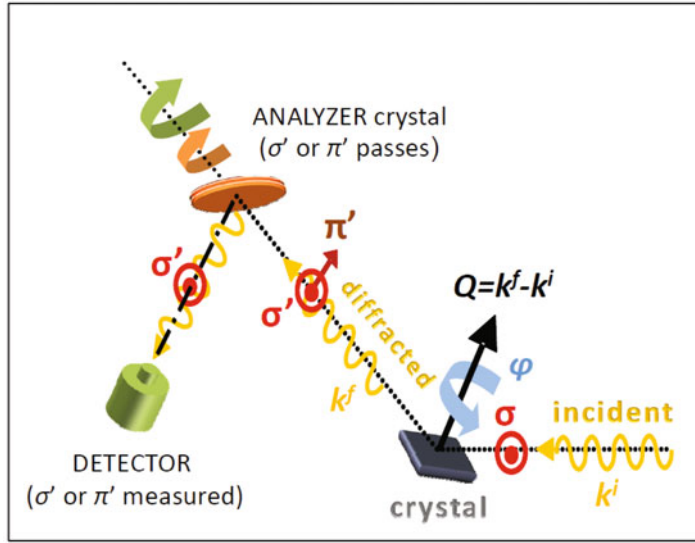
Fig. 2. Scheme of the experimental configuration used for recording the RXS spectra presented through this paper.

characteristic oscillation with π periodicity for these cubic manganites. This indicates a marked different anisotropy of the two types of Mn atoms involved. On the contrary, $(h/2,h/2,0)$ reflections in layered LSMO show a less pronounced azimuth dependence. We will later show that this is due to the different crystallographic space group. The dramatic enhancement (peak) or reduction (valley) of the resonant intensity at the Mn K edge depends on the crystal structure and on the specific reflection. This behaviour depends on the relative phase between the Thomson term and the anomalous one. When both are in phase a peak is observed whereas if they are out of phase a valley is found. This weak Thomson contribution is due to little atomic displacements with respect to the ideal tetragonal phase (as at $T > T_{\mathrm{SI}}$). Little variations of the Thomson contribution between theoretically equivalent superlattice weak permitted reflections as a function of $\boldsymbol{Q}$ that do not carry a phase sign can simply give rise to a different resonant/non resonant ratio, as in BSMO if we look at (030) and (050) reflections. The different anisotropy of the two Mn atoms was also demonstrated by the observation of a little reflected intensity in the $\sigma-\pi$' channel with $\pi/2$ periodicity [18].

We now move to the so-called OO reflections. Figure 4 shows the energy dependence of the reflections originated by the anisotropy of the anomalous scattering tensor in NSMO, BSMO and LSMO. We observe a strong Gaussian-shaped resonance at energies close to the Mn K edge in $(0,5/2,0)$ and $(5/4,5/4,0)$ reflections only in the rotated $(\sigma - \pi')$ channel, which identifies these half-integer reflections as structurally forbidden ones. Similarly to CO reflections, the azimuthal variation of these resonances shows a characteristic oscillation with π periodicity. We note that in this case, the behavior in both the cubic and layered perovskites is identical due to the markedly different anisotropy of the two types of atoms. The $\pi/2$ offset in the sucession of maxima/minima responds to the selection of a different "zero" reference axis. The resonant scattering at either $(0,k/2,0)$ or $(h/4,h/4,0)$ reflections does not depend on the $\boldsymbol{k}$ wavevector, i.e. it arises solely from a dd $(1s \rightarrow np)$ transition.

The temperature dependence of all (weak and forbidden) superstructural reflections here described shows that they are originated at the semiconductor-insulator (SI) phase transition. No intensity was found at $T > T_{\mathrm{SI}}$ [15,16,18].
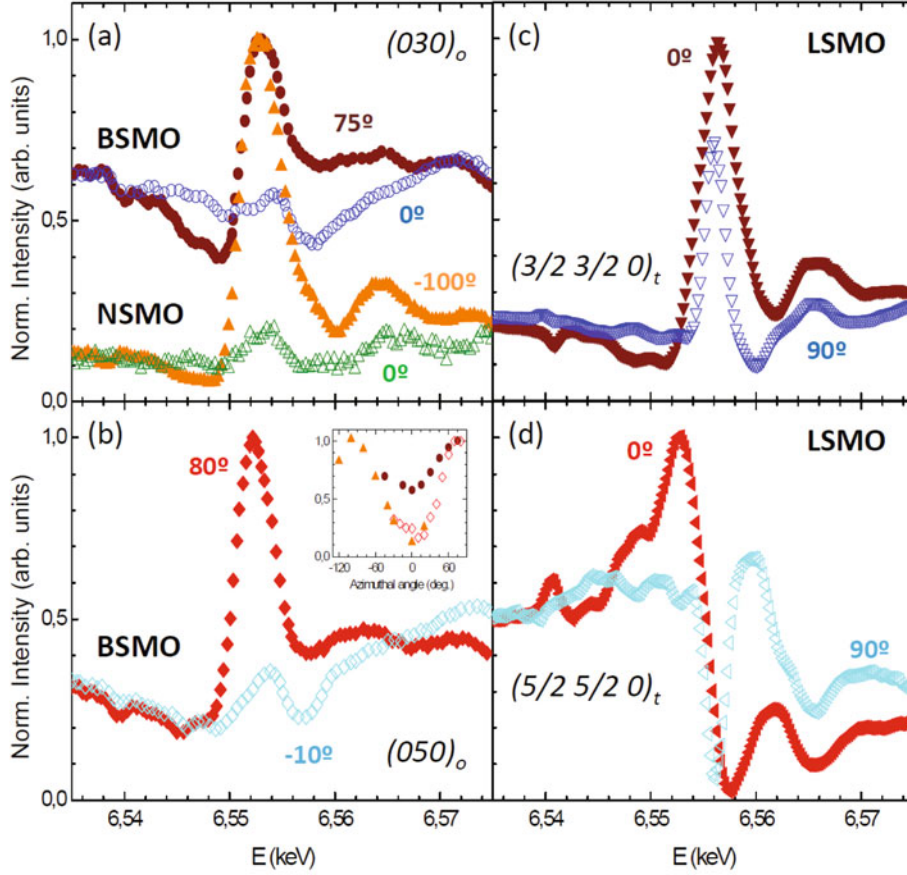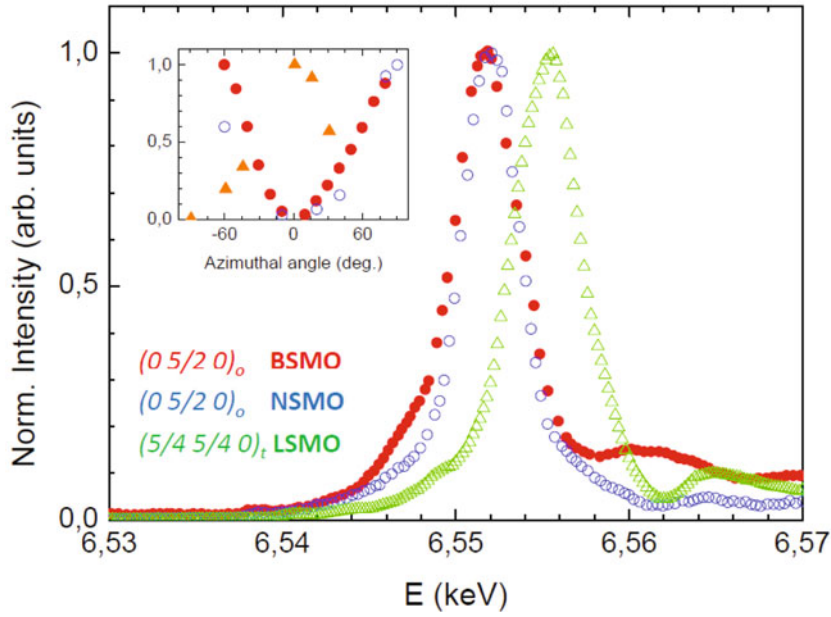
Fig. 3. CO reflections in BSMO, NSMO and layered LSMO at different azimuthal angles in the $\sigma - \sigma'$ polarization channel. The inset in (b) shows the azimuthal evolution of the intensity at the maximum for (030) (filled circles) and (050) (open diamonds) reflections of BSMO, and (030) (filled triangles) of NSMO. Subscripts o and t stand for orthorhombic and tetragonal, respectively.

We have used two methods for a quantitative analysis of the energy, azimuth and polarization dependences of the intensity of these reflections: the *semiempirical* approach and *ab initio* multiple scattering calculations.

In the semiempirical approach model, the atomic anomalous scattering factor of the Mn1 atom (Mn^{4+} in the ionic description) is considered as isotropic (it can be described by a diagonal tensor with $f_{xx} = f_{yy} = f_{zz} = f$) and the ASF of Mn2 (i.e. tetragonally distorted Mn^{3+}) is described by a diagonal tensor in the reference frame of the local distorted octahedron, with two equal in-plane components ($f_\perp$) and a different one along the tetragonal distortion direction, $f_\parallel$. A Thomson term $C_{h(k)}$ is included. Using the structure factor of the high temperature phase, the azimuth and polarization dependences of the studied reflections for cubic manganites are: [15, 16]

$$I_{\sigma\sigma'}(h00) = I_{\sigma\sigma'}(0k0) = [C_{h(k)} + 2(f_\perp - f)\cos^2\phi + (f_\perp + f_\parallel - 2f)\sin^2\phi]^2$$

$$I'_{\sigma\pi}(h00) = I'_{\sigma\pi}(0k0) = [(f_\perp + f_\parallel)\sin\phi\cos\phi\sin\theta]^2$$

$$I_{\sigma\sigma'}(0k/20) = 0$$

$$I_{\sigma\pi'}(0k/20) = [(f_\parallel - f_\perp)\sin\phi\cos\theta]^2.$$

Fig. 4. OO reflections in BSMO (red filled circles), NSMO (blue open circles) and layered LSMO (green open triangles) in the $\sigma - \pi$' channel. In the inset we depict the azimuthal evolution at the resonance of (0 5/2 0) in BSMO (filled circles) and NSMO (open circles), and (7/4 7/4 0) in LSMO (filled triangles).

And similar expressions can be deduced for the bidimensional case [18].

In order to determine the energy dependence, we consider that the atomic anomalous scattering diagonal terms produce a very similar spectral line shape for Mn1 and Mn2 in the crystal for both σ and π polarization. The main difference between the different components should be a rigid energy shift at the absorption edge. The XANES spectrum is directly proportional to the f'' term. More precisely, $f''(\omega) = [\omega\sigma_a]/[4\pi r_e c]$, where ω is the incident energy, σ_a the absorption cross section, r_e the electron radius and c the light velocity in vacuum. One then calculates f' straightforwardly via the Kramers-Kronig integral relation. In the semiempirical model the structure factor of reflections is calculated using the high temperature crystal structure. The low temperature structure is usually unknown and the non resonant intensity is accounted for by an *ad hoc* Thomson term. Thus, calculated intensities shall not be compared in an absolute scale. Within the rigid energy shift approximation, we can define the following relations between the different components of the anomalous scattering tensors: $f(E) = f_{anis}(E + \delta_{chem})$ and $f_{\perp}(E) = f_{\parallel}(E + \delta_{anis})$, where $f(E)$ represents the atomic anomalous scattering factor for Mn1, $f_{\parallel}$ and $f_{\perp}$ are the parallel and the perpendicular components of Mn2, and f_{anis} is the unpolarized anomalous scattering factor $(1/3)(2f_{\parallel} + f_{\perp})$ of Mn2. The two parameters, δ_{anis} and δ_{chem}, are a practical way of information on Mn1 and Mn2 atoms. On the one hand, δ_{chem} can be correlated with the formal valence of the atoms. Since the Mn K edge position in a Mn^{3+} reference sample is about 4.5 eV lower than that in a Mn^{4+}-based compound, this parameter can be used as a quantitative estimation of the charge disproportion between the two atoms. On the other hand δ_{anis} provides an estimation of the tetragonal distortion. The values of δ_{chem} for the studied samples range between 0.7 and 0.9 eV which yields a charge disproportion of 0.15–0.20 electrons. We note that for $Bi_{0.63}Sr_{0.37}MnO_3$ [17], the average Mn valence is 3.37 instead of 3.5.
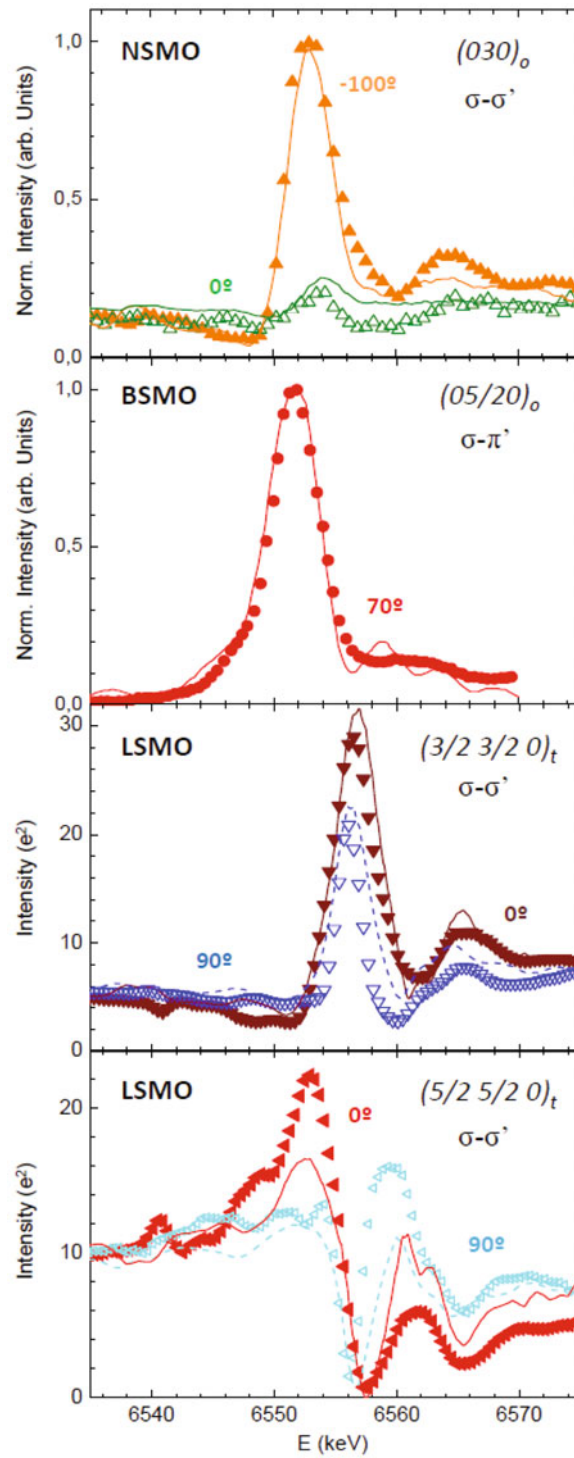
Fig. 5. Comparison between best-fit simulations using the semiempirical model (solid lines) and experimental spectra (symbols) of NSMO, BSMO and layered LSMO.
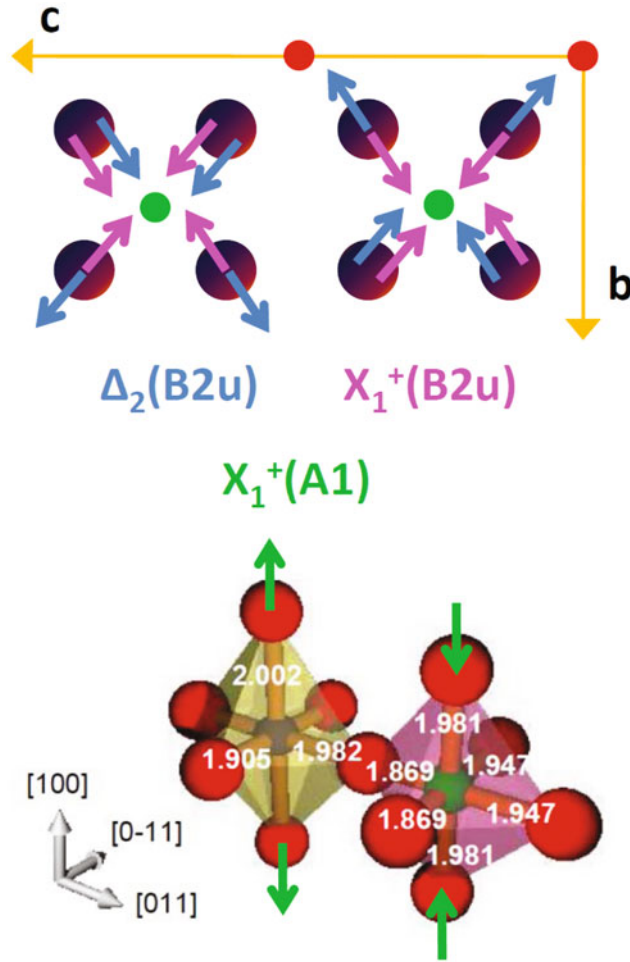
Fig. 6. Schematic picture of the movement associated to the three condensed modes acting on oxygen atoms in layered LSMO as derived from experimental XRD and RXS data, and the FDMNES analysis of the latter. Green and red balls refer to Mn2 and O atoms, respectively.

However, δ_{anis} ranges from 0.9 to 1.6 eV lower of that found in $LaMnO_3$ anisotropy [19]. In Fig. 5 we show the best-fit results on NSMO, BSMO and LSMO by using this semiempirical method. We note the nice agreement between experiments and simulations, which supports the adequacy of the approach performed.

The second method consists on calculating the RXS spectra by means of *ab initio* simulations. The FDMNES code allows calculating the X-ray absorption coefficient and the tensorial ASF from first principles as a function of the photon energy for the different crystallographic Mn sites. The intensity of resonant reflections is then calculated using these ASF for a finite cluster of atoms surrounding the absorbing one and the potential used is built on the basis of neutral atomic spheres. This approach qualitatively agrees with the experimental results [18] and has allowed us to determine the effect of the geometry on the anomalous part of the ASF. Needless to say, to carry out this kind of analysis a certain knowledge on the crystallographic structure of the ordered phase is necessary, which is unfortunately not frequently the case. In our last work on $La_{0.5}Sr_{1.5}MnO_4$ [18], we analyzed high-resolution synchrotron X-ray powder diffraction (XRD) data and RXS spectra in the frame of a symmetry-mode analysis

to determine the active modes that condensate at the semiconductor-insulator phase transition. The modes acting on the oxygen atoms that would account for the structural transformation are Δ_2(B2u), X_1^+ (B2u) and X_1^+ (A1) and their effect is schematically depicted in Fig. 6. More precisely, Δ_2(B2u) corresponds to a pseudo Jahn-Teller distortion (in the orthorhombic bc plane) on Mn1 sites, whereas X_1^+ (B2u) and X_1^+ (A1) modes produce an overall contraction at the Mn2 site and an expansion at Mn1. X_1^+ modes produce the appearance of superlattice $(h/2,h/2,0)$-type reflections in agreement with a checkerboard ordering of two different Mn sites. Δ_2(B2u) is also responsible for the anisotropic forbidden reflections. The energy dependence and absolute intensities of the RXS spectra were fitted using FDMNES, with the amplitude of the modes as fitting parameters. Other possible active modes were discarded on the basis of the multiple scattering calculations. More details can be found in Ref. [18]. The simulations are fairly good regarding the overall behaviour of the reflections and correctly reproduce the absolute and relative (resonant to non-resonant) intensities but they should not be considered as truly quantitative. The values of the refined atomic displacements are too low to be detected by high-resolution X-ray powder diffraction.

4 Conclusions and discussion

Resonant X-ray scattering is an experimental technique that permits to determine the electronic and structural characteristics of the so-called CO phases in half-doped manganites through the study of the energy, azimuth and polarization dependences of a few weak superlattice and/or symmetry forbidden reflections.

In several recent works, we have shown by means of RXS that the charge localized phase in half-doped manganites is well described by a checkerboard ordering of two non-equivalent Mn sites. Two types of superstructure reflections characterize this phase: i) permitted reflections with very low intensity originated by the alternating contraction and expansion of the local octahedron around Mn atoms, and ii) reflections that are forbidden by symmetry. The latter reflections inform us about an ordering of the local anisotropy in one of the Mn atoms, while weak permitted ones can be interpreted as a charge modulation on the Mn atoms. We have reported here on two methods to extract the relevant information contained in the spectra. First, the semiempirical phenomenological approach where parameters as the chemical shift and the anisotropic shift can be retrieved. δ_{chem} is directly correlated with the formal valence state of the atoms and in consequence, it provides a value of the formal charge segregation between different manganese sites. On the other hand, δ_{anis} is a measure of the local anisotropy around the Mn atom. The second method is based on a structural analysis of the manganite in the CO-OO phase. Since the atomic anomalous scattering factor mainly depends on the local geometry, *ab initio* calculations can help to refine the amplitudes of the condensing phonon modes responsible of the structural transition that lead to the charge localization. The application of this method can provide a more detailed information on the electronic and geometrical structure at low T but it also requires a previous guess on the actual low T structure. In this sense, a deep XRD study on the material at low and high T can complement RXS data and help in the refinement process. We used this method to analyze $La_{0.5}Sr_{1.5}MnO_4$ as further explained in Ref. [18].

To conclude, Mn K edge RXS results here presented discard the interpretation of mixed-valence manganites as a bimodal distribution of Mn^{3+} and Mn^{4+} valence states. Instead the so-called CO phase is consistent with a model in which atoms of the same chemical species in different crystallographic sites present an electronic

occupation mainly determined by the local geometrical structure. Structural distortions giving rise to different crystallographic sites would induce a different charge density on them and in some cases, an electronic anisotropy by lowering the local symmetry. Finally, we would like to stress that RXS has become a fundamental tool to determine the type of ordering and the low T structure in several cases, such as $Bi_{0.67}Sr_{0.33}MnO_3$ [17] and $La_{0.33}Sr_{0.67}FeO_3$ [31].

References

1. G. Materlik, J.C. Spark, K. Fisher, *Resonant Anomalous X-ray Scattering, Theory and Applications* (North-Holland/Elsevier Science B. V., Amsterdam, 1994)
2. D.C. Koningsberger, R. Prins, *X-ray Absorption: Principles, Application, Techniques of EXAFS, SEXAFS and XANES* (Wiley, New York, 1994)
3. H. Stragier, J.O. Cross, J.J. Rehr, L.B. Sorensen, C.E. Bouldin, J.C. Woicik, Phys. Rev. Lett. **21**, 3064 (1992)
4. M.G. Proietti, H. Renevier, J.L. Hodeau, J. García, J.F. Bérar, P. Wolfers, Phys. Rev. B. **59**, 5479 (1999)
5. G. Subías, J. García, J. Blasco, J. Herrero-Martín, M.C. Sánchez, J. Phys. Conf. Ser. **190**, 012085 (2009) and referentes therein
6. Y. Murakami, H. Kawada, H. Kawata, M. Tanaka, T. Arima, Y. Moritomo, Y. Tokura, Phys. Rev. Lett. **80**, 1932 (1998)
7. Y. Murakami, J.P. Hill, D. Gibbs, M. Blume, I. Koyama, M. Tanaka, H. Kawata, T. Arima, Y. Tokura, K. Hirota, Y. Endoh, Phys. Rev. Lett. **81**, 582 (1998)
8. M. Zimmermann, J.P. Hill, D. Gibbs, M. Blume, D. Casa, B. Keimer, Y. Murakami, Y. Tomioka, Y. Tokura, Phys. Rev. Lett. **83**, 4872 (1999)
9. G. Subias, J. García, J. Blasco, J. Herrero-Martín, M.C. Sánchez, J. Orna, L. Morellón, J. Synchr. Rad. **19**, 159 (2012)
10. K.J. Thomas, J.P. Hill, Y.J. Kim, S. Grenier, P. Abbamonte, L. Venema, A. Rusydi, Y. Tomioka, Y. Tokura, D.F. McMorrow, M. van Veenendaal, Phys. Rev. Lett. **92**, 237204 (2004)
11. S.B. Wilkins, N. Stoji'c, T.A. Beale, N. Binggeli, C.W. Castleton, P. Bencok, D. Prabhakaran, A.T. Boothroyd, P.D. Hatton, M. Altarelli, Phys. Rev. B **71**, 245102 (2005)
12. J. Herrero-Martín, J. García, G. Subías, J. Blasco, M.C. Sánchez, S. Stanescu, Phys. Rev. B **73**, 224407 (2006)
13. U. Staub, V. Scagnoli, A.M. Mulders, M. Janousch, Z. Honda, J.M. Tonnerre, Europhys. Lett. **76**, 926 (2006)
14. J. García, M.C. Sánchez, J. Blasco, G. Subías, M.G. Proietti, J. Phys.: Condens. Matter **13**, 3243 (2001)
15. J. Herrero-Martín, J. García, G. Subías, J. Blasco, M.C. Sánchez, Phys. Rev. B **70**, 024408 (2004)
16. G. Subías, J. García, P. Beran, M. Nevriva, M.C. Sánchez, J.L. García-Muñoz, Phys. Rev. B **73**, 205107 (2006)
17. G. Subías, M.C. Sánchez, J. García, J. Blasco, J. Herrero-Martín, C. Mazzoli, P. Beran, M. Nevriva, J.L. García-Muñoz, J. Phys.: Condens. Matter **20**, 235211 (2008)
18. J. Herrero-Martín, J. Blasco, J. García, G. Subías, C. Mazzoli, Phys. Rev. **83**, 184101 (2011)
19. G. Subías, J. Herrero-Martín, J. García, J. Blasco, C. Mazzoli, K. Hatada, S. Di Matteo, C. R. Natoli, Phys. Rev. B **75**, 235101 (2007)
20. M. Benfatto, Y. Joly, C.R. Natoli, Phys. Rev. Lett. **83**, 636 6 (1999)
21. D.H. Templeton, L.K. Templeton, Acta Cryst. A **36**, 237 (1980)
22. Y. Joly, Phys. Rev. B **63**, 125120 (2001)
23. M. Blume, *Resonant Anomalous X-ray Scattering, Theory and Applications*, edited by G. Materlik, C.J. Spark, K. Fisher (North-Holland/Elsevier Science B. V., Amsterdam, 1994), p. 495

24. V.E. Dmitrienko, K. Ishida, A. Kirfel, E.N. Ovchinnikova, Acta Crystallogr. Sect. A **61**, 481 (2005)
25. E. Dagotto, J. Hotta, A. Moreo, Phys. Rep. **344**, 1 (2001)
26. M.B. Salamon, M. Jaime, Rev. Mod. Phys. **73**, 583 (2001)
27. J. Goodenough, Phys. Rev. **100**, 564 (1955)
28. P.G. Radaelli, D.E. Cox, M. Marezio, S.W. Cheong, Phys. Rev. B **55**, 3015 (1997)
29. S. Larochelle, A. Mehta, L. Lu, P.K. Mang, O.P. Vajk, N. Kaneko, J.W. Lynn, L. Zhou, M. Greven, Phys. Rev. B **71**, 024435 (2005)
30. D. Sneff, P. Reutler, M. Braden, O. Friedt, D. Bruns, A. Cousson, F. Bouree, M. Merz, B. Bushner, A. Recovleski, Phys. Rev. B **71**, 024425 (2005)
31. J. Herrero-Martín, G. Subías, J. García, J. Blasco, M.C. Sánchez, Phys. Rev. B **79**, 045121 (2009)